

Giant Goos-Hänchen shifts with high reflection driven by Fabry-Perot quasibound states in the continuum in double-layer gratings


Feng Wu^{1,*}, Tingting Liu^{2,3}, Ma Luo¹, Hongju Li⁴, and Shuyuan Xiao^{2,3,†}

¹*School of Optoelectronic Engineering, Guangdong Polytechnic Normal University, Guangzhou 510665, China*

²*Institute for Advanced Study, Nanchang University, Nanchang 330031, China*

³*Jiangxi Key Laboratory for Microscale Interdisciplinary Study, Nanchang University, Nanchang 330031, China*

⁴*School of Physics, Hefei University of Technology, Hefei 230009, China*

 (Received 8 January 2024; revised 20 February 2024; accepted 27 February 2024; published 11 March 2024)

Herein, we achieve giant Goos-Hänchen (GH) shifts driven by Fabry-Perot quasibound states in the continuum (quasi-BICs) in double-layer gratings. Based on the hybrid coupling model, the linewidths of two resonant modes in a double-layer grating are determined *entirely* by the far-field coupling strength. When the vertical distance between two single-layer gratings satisfies the Fabry-Perot resonant condition, the linewidth of one of the resonant modes vanishes, giving rise to a Fabry-Perot BIC. The Q factor of the Fabry-Perot quasi-BIC can be tuned over a wide range by the vertical distance between single-layer two gratings. Driven by the angle-sensitive and ultrastrong resonant properties of the Fabry-Perot quasi-BIC, the GH shift can be significantly enhanced to the order of $10^3\lambda$, together with high reflection. Compared with the reported works on giant GH shifts assisted by momentum-mismatch-driven quasi-BICs in dimerized gratings [*Phys. Rev. Appl.* **12**, 014028 (2019); *Phys. Rev. A* **104**, 023518 (2021)], the proposed scheme greatly reduces the difficulty in experiments. Our work not only provides a feasible recipe to observe quasi-BIC-driven giant GH shifts, but also facilitates the development of high-performance sensors and optical switches.

DOI: [10.1103/PhysRevB.109.125411](https://doi.org/10.1103/PhysRevB.109.125411)

I. INTRODUCTION

When a light beam is totally reflected by an interface between two media, it experiences a lateral displacement relative to its incident position. This displacement is known as the Goos-Hänchen (GH) shift [1]. The physics [2–13] and applications [14–24] of the GH shift have been widely explored over the past decades. Particularly, the enhancement of the GH shift has been a long-standing goal in physical optics. In the light of the stationary-phase approach, the GH shift is proportional to the change rate of the reflection phase with respect to the incident angle [25]. Consequently, the GH shift can be enhanced by optical resonances. In the past two decades, researchers have exploited the Brewster effects [26–28], surface plasmon polaritons [29–32], Fabry-Perot resonances [33–35], Bloch surface waves [36,37], and Tamm plasmon polaritons [38–40] to effectively enhance the GH shift. Nevertheless, the resonant strengths of the above optical resonances are limited. As a result, the GH shift in the above reported works can only be enhanced to smaller than or equal to the order of $10^3\lambda$ [26–40]. It is hard to observe giant GH shifts empowered by the conventional optical resonances in experiments.

Bound states in the continuum (BICs), singular states embedded in continuous spectra, open a new chapter in nanophotonics [41–44]. After introducing parameter perturbation, BICs convert into quasi-BICs with ultrastrong resonant

strengths [45]. Over the last decade, various nanostructures have been designed to support quasi-BICs, including photonic crystal slabs [46–50], metasurfaces [51–57], and gratings [58–64]. In addition, quasi-BICs have disclosed applications in high-performance sensors [65,66], chiralities [67–70], and nonlinear devices [71–73]. Recently, researchers theoretically enhanced the GH shift to the order of $10^4\lambda$ driven by the quasi-BICs in dimerized gratings [74–77]. This special category of BICs in dimerized gratings can be called as momentum-mismatch-driven BICs since they originate from momentum mismatch [78]. The unit cell of the dimerized gratings is composed of two dielectric ridges and two air grooves. Nevertheless, the Q factor of the quasi-BIC in the dimerized grating is determined by the *in-plane* distance between two dielectric ridges or two air grooves [74–78]. In the etching process, it is difficult to accurately control the in-plane distance, which greatly hinders the observation of giant GH shift in experiments. In 2023, Jin *et al.* fabricated the dimerized gratings and experimentally observed the quasi-BICs at near-infrared wavelengths [79]. However, the measured Q factors of the quasi-BICs in the dimerized gratings in Ref. [79] are only on the order of 10^2 (<250) [79]. So far, no literature has observed giant or large GH shifts driven by quasi-BICs in dimerized gratings or other structures.

As a special class of BICs, Fabry-Perot BICs in double-layer gratings have attracted extensive attention [80–87]. Interestingly, the Q factor of the Fabry-Perot quasi-BIC in a double-layer grating can be tuned by the *out-of-plane* distance between two single-layer gratings [80–87], which greatly reduces the difficulty to observe higher Q factors in experiments

*fengwu@gpnu.edu.cn

†syxiao@ncu.edu.cn

compared with quasi-BICs in dimerized gratings. In 2020, Xu *et al.* fabricated the double-layer gratings and experimentally observed Fabry-Perot quasi-BICs at near-infrared wavelengths [88]. The measured Q factors of the Fabry-Perot quasi-BICs in the double-layer gratings reaches the order of 10^3 (>5000) [88], which is at least one order of magnitude higher than those of quasi-BICs in dimerized gratings. It indicates that Fabry-Perot quasi-BICs in double-layer gratings may be a better candidate for experimentally observing giant GH shifts compared with quasi-BICs in dimerized gratings. In this paper, we explore the possibility to achieve giant GH shifts driven by Fabry-Perot quasi-BICs in double-layer gratings. Based on the hybrid coupling model (HCM), the linewidths of two resonant modes in a double-layer grating are determined *entirely* by the far-field coupling strength. Our results show that the Q factor of the Fabry-Perot quasi-BIC can be tuned over a wide range by the out-of-plane distance between two single-layer gratings. Specifically, as the out-of-plane distance between two single-layer gratings changes from 100 to 240 nm, the Q factor of the Fabry-Perot quasi-BIC rapidly increases from 2.14×10^1 to 7.02×10^4 . Driven by the angle-sensitive and ultrastrong resonant properties of the Fabry-Perot quasi-BIC, the GH shift can be significantly enhanced to the order of $10^3\lambda$, together with high reflection. Compared with the reported works on quasi-BIC-driven giant GH shift in dimerized gratings [74–77], the proposed scheme greatly reduces the difficulty in experiments. Our work not only provides a feasible route to observing quasi-BIC-driven giant GH shifts in experiments, but also facilitates the development of high-performance sensors and optical switches. It is worth pointing out that researchers achieved BICs in triple-layer structures composed of two epsilon-near-zero layers and a dielectric layer recently [89,90]. The double-layer grating proposed in this work can also be viewed as a triple-layer structure when considering the middle air layer.

The rest of this paper is organized as follows. In Sec. II, we discuss the Fabry-Perot BICs in the double-layer gratings based on a HCM comprising near- and far-field couplings. In Sec. III, we achieve giant GH shifts driven by the Fabry-Perot quasi-BICs in the double-layer gratings. Eventually, the conclusion is given in Sec. IV.

II. FABRY-PEROT BICS IN DOUBLE-LAYER GRATINGS

In this section, we discuss the Fabry-Perot BICs in the double-layer gratings based on a HCM comprising near- and far-field couplings. In Sec. II A, we give the hybrid coupling model comprising near- and far-field couplings. In Sec. II B, we realize a Fabry-Perot BIC in the double-layer grating at oblique incidence. In Sec. II C, we investigate the angle-dependent property of the Fabry-Perot BIC.

A. Hybrid coupling model for double-layer gratings

Figure 1(a) schematically shows the double-layer grating consisting of two identical single-layer gratings. Suppose that a plane wave obliquely launches onto the double-layer grating with an incident angle θ . The period and height of the single-layer grating are denoted by p and h , respectively. The refractive indices of the high- and low-index materials

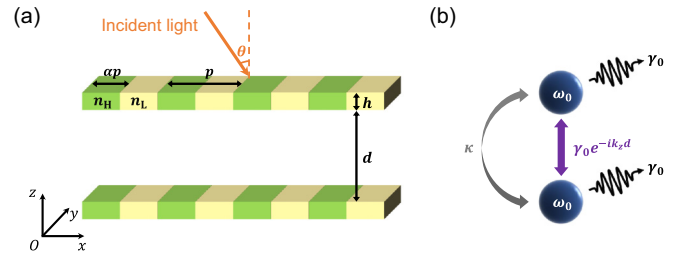


FIG. 1. (a) Schematic of the double-layer grating consisting of two identical single-layer gratings. (b) HCM comprising near- and far-field couplings.

denoted by n_H and n_L , respectively. The filling ratio of the high-index material is denoted by α . The vertical distance between two single-layer gratings is denoted by d . Owing to the guided mode resonance, each single-layer grating can be treated as a resonator with a resonant angular frequency ω_0 and a radiative loss γ_0 [91]. Therefore, the optical response of the double-layer grating can be described by a HCM comprising near- and far-field coupling, as shown in Fig. 1(b). First, we view the double-layer grating as a closed system, the Hamiltonian can be expressed as [41]

$$H = \begin{bmatrix} \omega_0 & \kappa \\ \kappa & \omega_0 \end{bmatrix} + i \begin{bmatrix} \gamma_0 & \gamma_0 e^{-ik_z d} \\ \gamma_0 e^{-ik_z d} & \gamma_0 \end{bmatrix}, \quad (1)$$

where κ represents the near-field coupling strength and $\gamma_0 e^{-ik_z d}$ represents the far-field coupling strength. It should be noted that the overlapping of localized evanescent fields of two single resonators contributes to the near-field coupling. Hence, the near-field coupling strength is pure real [92–94]. Besides, the near-field coupling strength decreases as the distance between two resonators increases [92–94].

Then, two complex eigen angular frequencies can be obtained:

$$\omega_{\pm} = \omega_0 \pm \kappa + i\gamma_0(1 \pm e^{-ik_z d}). \quad (2)$$

The angular frequency positions of two resonant modes are determined by the real parts of two complex eigen angular frequencies, i.e.,

$$\text{Re}(\omega_{\pm}) = \omega_0 \pm [\kappa + \gamma_0 \sin(k_z d)]. \quad (3a)$$

The linewidths of two resonant modes are determined by the imaginary parts of two complex eigen angular frequencies, i.e.,

$$\text{Im}(\omega_{\pm}) = \gamma_0[1 \pm \cos(k_z d)]. \quad (3b)$$

For oblique incidence, the propagating phase between two single-layer gratings can be expressed as

$$k_z d = k_0 d \cos\theta = \frac{\omega_0}{c} d \cos\theta. \quad (4)$$

Substituting Eq. (4) into Eqs. (3a) and (3b), we have

$$\text{Re}(\omega_{\pm}) = \omega_0 \pm \left[\kappa + \gamma_0 \sin\left(\frac{\omega_0}{c} d \cos\theta\right) \right], \quad (5a)$$

$$\text{Im}(\omega_{\pm}) = \gamma_0 \left[1 \pm \cos\left(\frac{\omega_0}{c} d \cos\theta\right) \right]. \quad (5b)$$

According to Eq. (5b), the vertical distance between two single-layer gratings strongly determines the linewidths of two resonant modes. Particularly, when the vertical distance between two single-layer gratings satisfies

$$\frac{\omega_0}{c}d\cos\theta = \pi, \quad (6)$$

the angular frequency positions and linewidths of two resonant modes become

$$\text{Re}(\omega_{\pm}) = \omega_0 \pm \kappa, \quad (7a)$$

$$\text{Im}(\omega_{\pm}) = \gamma_0(1 \mp \mp 1). \quad (7b)$$

According to Eqs. (7a) and (7b), the resonant mode ω_+ is located at the angular frequency position $\omega_0 + \kappa$ with a vanishing linewidth, leading to a Fabry-Perot BIC. The resonant mode ω_- is located at the angular frequency position $\omega_0 - \kappa$ with the linewidth $2\gamma_0$.

Now, we view the double-layer grating as an open system to obtain the expression of the reflectance spectrum. Suppose that an electromagnetic wave \tilde{S}_0 impinges on the double-layer grating. According to the temporal coupled-mode theory [95], the dynamic equations for two resonant modes (\tilde{a}_1 and \tilde{a}_2) can be given by

$$\frac{d\tilde{a}_1}{dt} = (i\omega_0 - \gamma_0)\tilde{a}_1 + i\kappa\tilde{a}_2 + i\sqrt{\gamma_0}\tilde{S}_0 - \gamma_0e^{-i\varphi}\tilde{a}_2, \quad (8a)$$

$$\frac{d\tilde{a}_2}{dt} = (i\omega_0 - \gamma_0)\tilde{a}_2 + i\kappa\tilde{a}_1 + i\sqrt{\gamma_0}e^{-i\varphi}\tilde{S}_0 - \gamma_0e^{-i\varphi}\tilde{a}_1, \quad (8b)$$

where κ represents the near-field coupling strength and $\gamma_0e^{-i\varphi}$ represents the far-field coupling strength with φ being the phase term.

For the time-harmonic case, we have

$$\tilde{a}_m = A_m e^{i\omega t} \quad (m = 1, 2), \quad (9a)$$

$$\tilde{S}_0 = S_0 e^{i\omega t}, \quad (9b)$$

where ω and t represent the angular frequency and time, respectively. Under the steady-state condition, i.e., $dA_m/dt = 0$, Eqs. (8a) and (8b) reduce to

$$[i(\omega_0 - \omega) - \gamma_0]A_1 + (i\kappa - \gamma_0e^{-i\varphi})A_2 + i\sqrt{\gamma_0}S_0 = 0, \quad (10a)$$

$$(i\kappa - \gamma_0e^{-i\varphi})A_1 + [i(\omega_0 - \omega) - \gamma_0]A_2 + i\sqrt{\gamma_0}e^{-i\varphi}S_0 = 0. \quad (10b)$$

The solutions of Eqs. (10a) and (10b) are

$$A_1 = \frac{i\sqrt{\gamma_0}e^{-i\varphi}(i\kappa - \gamma_0e^{-i\varphi}) - i\sqrt{\gamma_0}[i(\omega_0 - \omega) - \gamma_0]}{[i(\omega_0 - \omega) - \gamma_0]^2 - (i\kappa - \gamma_0e^{-i\varphi})^2}S_0, \quad (11a)$$

$$A_2 = \frac{i\sqrt{\gamma_0}(i\kappa - \gamma_0e^{-i\varphi}) - i\sqrt{\gamma_0}e^{-i\varphi}[i(\omega_0 - \omega) - \gamma_0]}{[i(\omega_0 - \omega) - \gamma_0]^2 - (i\kappa - \gamma_0e^{-i\varphi})^2}S_0. \quad (11b)$$

Hence, the reflection coefficient of the double-layer grating can be determined by [95]

$$r(\omega) = \frac{i\sqrt{\gamma_0}A_1 + i\sqrt{\gamma_0}e^{-i\varphi}A_2}{S_0}. \quad (12)$$

Finally, the reflectance of double-layer grating can be given by

$$R(\omega) = |r(\omega)|^2 = \left| \frac{i\sqrt{\gamma_0}A_1 + i\sqrt{\gamma_0}e^{-i\varphi}A_2}{S_0} \right|^2. \quad (13)$$

By fitting the reflectance spectrum, we can obtain the values of the near-field coupling strength κ and the phase term of the far-field coupling strength φ .

B. Fabry-Perot BICs in double-layer gratings at oblique incidence

In this subsection, we realize a Fabry-Perot BIC in the double-layer grating at oblique incidence. The incident angle is set to be $\theta = 3^\circ$. To make the reflectance spectrum of the single-layer grating satisfies the symmetric Lorentz line shape, the refractive indices of the high- and low-index materials are set to be $n_H = 2$ and $n_L = 1.8$, respectively. The filling ratio of the high-index material is set to be $\alpha = 0.5$. The period and height of the single-layer grating are set to be $p = 332$ nm and $h = 134$ nm, respectively. Based on the rigorous couple-wave analysis (RCWA) [96], we calculate the reflectance spectrum of the single-layer grating at oblique incidence ($\theta = 3^\circ$) for transverse electric (TE) polarization, as shown by the blue solid line in Fig. 2(a). To extract the values of ω_0 and γ_0 , we fit the reflectance spectrum by the following single resonator model (SRM) [97]:

$$R(\omega) = \frac{\gamma_0^2}{(\omega - \omega_0)^2 + \gamma_0^2}. \quad (14)$$

The pink dashed line in Fig. 2(a) represents the fitted reflectance spectrum. Then, we obtain $\omega_0 = 3.7025 \times 10^{15}$ Hz and $\gamma_0 = 0.0033 \times 10^{15}$ Hz.

Substituting $\omega_0 = 3.7025 \times 10^{15}$ Hz and $\theta = 3^\circ$ into Eq. (6), we can obtain the vertical distance between two single-layer gratings for the Fabry-Perot BIC at oblique incidence ($\theta = 3^\circ$)

$$d_{\text{BIC}} = \frac{c\pi}{\omega_0 \cos\theta} = 254.9 \text{ nm}. \quad (15)$$

Then, we calculate the reflectance spectra of the double-layer gratings with different distances between two single-layer gratings at oblique incidence ($\theta = 3^\circ$) for TE polarization based on the RCWA, as shown in by the blue solid lines in Fig. 2(b). As demonstrated, a Lorentz resonance and a Fano resonance occur in the reflectance spectrum, which is consistent with Ref. [98]. The broad Lorentz resonance corresponds to the resonant mode ω_- . The narrow Fano resonance corresponds to the resonant mode ω_+ , i.e., the Fabry-Perot quasi-BIC. As the vertical distance between two single-layer gratings increases from 160 to 220 nm, the linewidth of the Fabry-Perot quasi-BIC reduces rapidly. According to the finite element method via commercially available software COMSOL Multiphysics, we simulate the electric field distributions at the reflectance peaks of the Fabry-Perot quasi-BICs, as shown by the insets in Fig. 2(b). The intensity of the local electric field is normalized to that of the incident electric field. As the vertical distance between two single-layer gratings increases from 160 to 220 nm, the maximum electric field

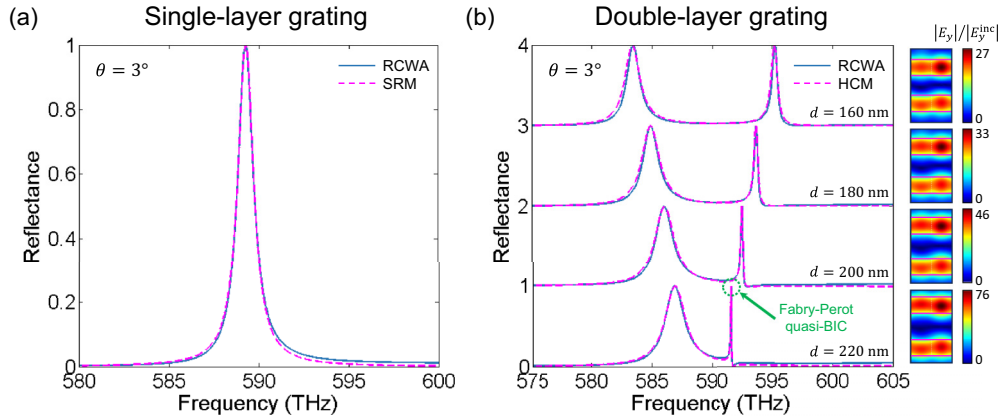


FIG. 2. (a) Reflectance spectra of the single-layer grating at oblique incidence ($\theta = 3^\circ$) for TE polarization. Blue solid line represents the reflectance spectrum calculated by the RCWA. Pink dashed line represents the reflectance spectrum fitted by the SRM. (b) Reflectance spectra of the double-layer gratings with different distances between two single-layer gratings at oblique incidence ($\theta = 3^\circ$) for TE polarization. Blue solid line represents the reflectance spectrum calculated by the RCWA. Pink dashed line represents the reflectance spectrum fitted by the HCM. Inset represents the electric field distribution at the reflectance peak of the Fabry-Perot quasi-BIC. The intensity of the local electric field is normalized to that of the incident electric field.

intensity increases rapidly, indicating that the resonant strength of the Fabry-Perot quasi-BIC increases rapidly.

To obtain the values of the near-field coupling strength κ and the phase term of the far-field coupling strength φ , we fit the reflectance spectra with the HCM [i.e., Eq. (13)]. The fitted reflectance spectra are shown by the pink dashed lines in Fig. 2(b). The reflectance spectra fitted by the HCM agree well with those calculated by the RCWA. The fitted parameters of the HCM are given in Table I.

As we mentioned in the introduction section, the Q factor of the quasi-BIC in the dimerized grating is determined by the in-plane distance between two dielectric ridges or two air grooves [74–78]. On the contrary, the Q factor of the Fabry-Perot quasi-BIC in the double-layer grating proposed in this work demonstrates a superior robustness when shifting one of the single-layer gratings in plane (details can be seen in Sec. I of the Supplemental Material [99]).

Next, we give the dependence of the Q factor of the Fabry-Perot quasi-BIC on the vertical distance between two single-layer gratings at oblique incidence ($\theta = 3^\circ$) for TE polarization, as shown in Fig. 3. When the vertical distance between two single-layer gratings $d = 100$ nm, the Q factor of the Fabry-Perot quasi-BIC is only 2.14×10^1 . As the vertical distance between two single-layer gratings gradually approaches d_{BIC} , the Q factor of the Fabry-Perot quasi-BIC increases rapidly. When the vertical distance between two single-layer gratings $d = 240$ nm, the Q factor of the

Fabry-Perot quasi-BIC reaches 7.02×10^4 . The frequency of the Fabry-Perot BIC at oblique incidence ($\theta = 3^\circ$) for TE polarization can be obtained as $f_{\text{BIC}} = 590.94$ THz.

It should be noted that the Q factor of the symmetry-protected quasi-BIC and asymmetric parameter β satisfy the quadratic inverse law, i.e., $Q \propto 1/\beta^2$ [51]. However, the quasi-BIC achieved in this work belongs to Fabry-Perot quasi-BICs instead of symmetry-protected quasi-BICs. Therefore, the Q factor of the quasi-BIC and the vertical distance between two single-layer gratings does not satisfy the quadratic inverse law. According to Eqs. (5a) and (5b), the Q factor of the Fabry-Perot quasi-BIC and the vertical distance between two single-layer gratings approximately satisfy the relationship

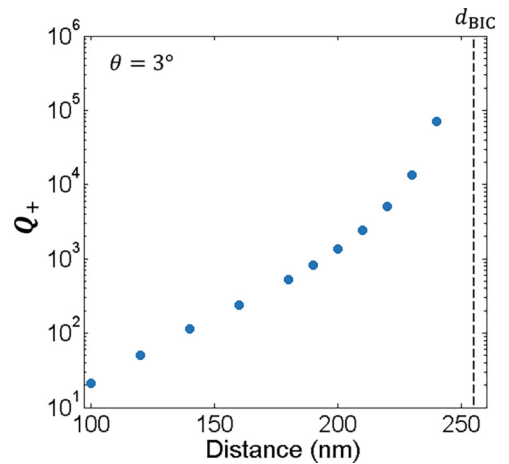


FIG. 3. Dependence of the Q factor of the Fabry-Perot quasi-BIC (Q_+) on the vertical distance between two single-layer gratings at oblique incidence ($\theta = 3^\circ$) for TE polarization. Black dashed line represents the vertical distance between two single-layer gratings for the Fabry-Perot BIC $d_{\text{BIC}} = 254.9$ nm.

TABLE I. Fitted parameters of the HCM.

d	κ	φ
160 nm	0.0344×10^{15} Hz	0.640π
180 nm	0.0254×10^{15} Hz	0.728π
200 nm	0.0187×10^{15} Hz	0.811π
220 nm	0.0138×10^{15} Hz	0.890π

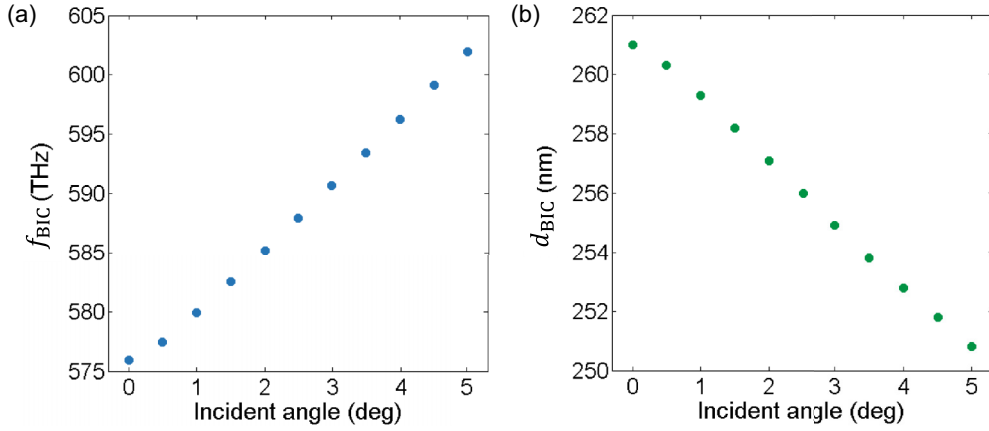


FIG. 4. (a) Dependence of the frequency of the Fabry-Perot BIC on the incident angle. (b) Dependence of the vertical distance between two single-layer gratings for Fabry-Perot BIC on the incident angle.

below:

$$Q_+ = \frac{1 \operatorname{Re}(\omega_+)}{2 \operatorname{Im}(\omega_+)} = \frac{\omega_0 + \kappa + \gamma_0 \sin\left(\frac{\omega_0}{c} d \cos\theta\right)}{2\gamma_0 \left[1 + \cos\left(\frac{\omega_0}{c} d \cos\theta\right)\right]}. \quad (16)$$

Notice that the near-field coupling strength κ in Eq. (16) is a function of the vertical distance between two single-layer gratings d .

C. Angle-dependent property of Fabry-Perot BICs in double-layer gratings

In this subsection, we investigate the angle-dependent property of the Fabry-Perot BIC in the double-layer grating. Figure 4(a) gives the dependence of the frequency of the Fabry-Perot BIC on the incident angle. As the incident angle increases from 0° to 5° , the frequency of the Fabry-Perot BIC gradually increases from 575.95 to 601.97 THz. According to Eq. (6), we calculate the dependence of the vertical distance between two single-layer gratings for the Fabry-Perot BIC on the incident angle, as shown in Fig. 4(b). As the incident angle increases from 0° to 5° , the vertical distance between two single-layer gratings for the Fabry-Perot BIC gradually decreases from 261.0 to 250.8 nm. Clearly, the Fabry-Perot BIC is angle sensitive. When the vertical distance between two single-layer gratings deviates from d_{BIC} , the angle-sensitive Fabry-Perot BIC turns into the angle-sensitive Fabry-Perot quasi-BIC, which thus provides us a possibility to significantly enhance the GH shift.

III. GIANT GH SHIFTS DRIVEN BY FABRY-PEROT QUASI-BICS

In this section, we utilize the angle-sensitive Fabry-Perot quasi-BIC to significantly enhance the GH shift at $\theta = 3^\circ$ under TE polarization. For $\theta = 3^\circ$, the vertical distance between two single-layer gratings can be calculated by Eq. (15), i.e., $d_{\text{BIC}} = 254.9$ nm. In Sec. II, we ignore the material and scattering losses of the high- and low-index materials of the double-layer grating. However, the material and scattering losses will be induced in the fabrication process. By fitting the measured reflectance spectrum of a HfO_2 (hafnium dioxide) grating in Ref. [91], the effective extinction coefficient of

HfO_2 contributed by the material and scattering losses can be obtained as $\operatorname{Im}(n) = 3 \times 10^{-5}$. Now, we consider the material and scattering losses and reselect the refractive indices of the high- and low-index materials of the double-layer grating as $n_{\text{H}} = 2 + 3 \times 10^{-5}i$ and $n_{\text{L}} = 1.8 + 3 \times 10^{-5}i$, respectively.

First, we set the vertical distance between two single-layer gratings as $d = 160$ nm, which is far from $d_{\text{BIC}} = 254.9$ nm. Figure 5 gives the reflectance spectra of the double-layer grating at $\theta = 2^\circ$, 3° , and 4° for TE polarization. As the incident angle increases from 2° to 4° , the reflectance peak of the Fabry-Perot quasi-BIC gradually shifts from 590.05 to 600.57 THz. When $\theta = 3^\circ$, the reflectance peak of the Fabry-Perot quasi-BIC is located at $f_0 = 595.25$ THz, which is denoted by the purple dashed line.

Figure 6(a) gives the reflectance angular spectrum of the double-layer grating at the frequency of the reflectance peak of the Fabry-Perot quasi-BIC $f_0 = 595.25$ THz for TE polarization. Owing to the angle-sensitive property of the Fabry-Perot quasi-BIC, an asymmetric Fano-like lineshape

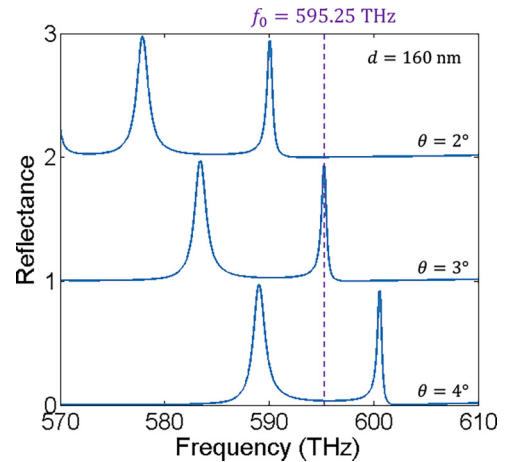


FIG. 5. Reflectance spectra of the double-layer grating at $\theta = 2^\circ$, 3° , and 4° for TE polarization. The vertical distance between two single-layer gratings is set to be $d = 160$ nm. Purple dashed line represents the frequency of the reflectance peak of the Fabry-Perot quasi-BIC $f_0 = 595.25$ THz.

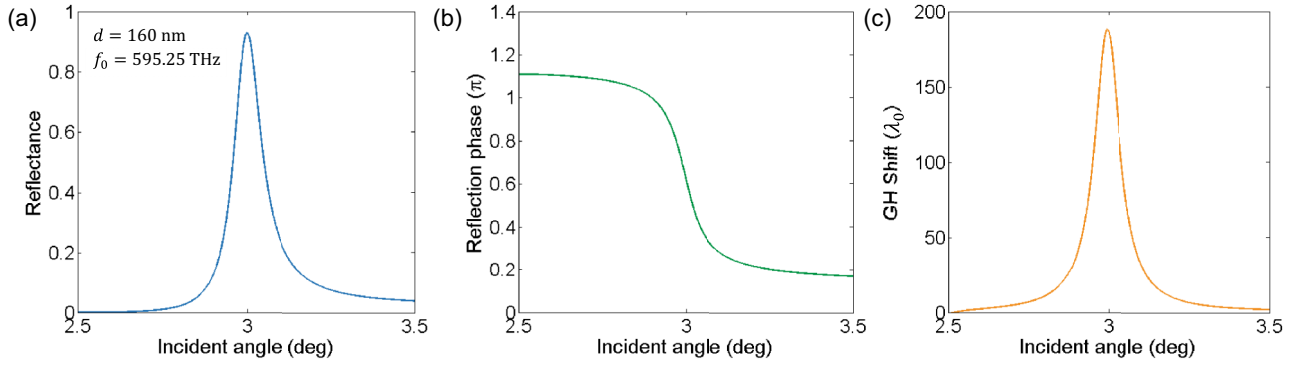


FIG. 6. (a) Reflectance, (b) reflection phase, and (c) GH shift angular spectra of the double-layer grating at the frequency of the reflectance peak of the Fabry-Perot quasi-BIC $f_0 = 595.25 \text{ THz}$ for TE polarization. The vertical distance between two single-layer gratings is set to be $d = 160 \text{ nm}$.

occurs at the resonant angle $\theta = 3^\circ$ in the reflectance angular spectrum. Based on the stationary-phase approach [34], the GH shift when the incident light beam is a quasi-plane wave can be calculated by

$$s_{\text{GH}} = -\frac{\lambda_0}{2\pi} \frac{\partial \varphi_r}{\partial \theta}, \quad (17)$$

where φ_r represents the reflection phase. In Fig. 6(b), we give the corresponding reflection phase angular spectrum. Obviously, the reflection phase changes sharply at the resonant angle $\theta = 3^\circ$. According to Eq. (17), we calculate the corresponding GH shift angular spectrum, as shown in Fig. 6(c). Owing to the sharp reflection phase change, the GH shift is enhanced to $188.3\lambda_0$ at the resonant angle $\theta = 3^\circ$. Importantly, the GH shift reaches its maximum at the reflectance peak, which can be more easily detected in experiments compared with large GH shifts driven by conventional transmission-type resonances. Specifically, the reflectance of the reflectance peak reaches 93.0%.

Then, we investigate the GH shift when the vertical distance between two single-layer gratings is $d = 220 \text{ nm}$ (details can be seen in Sec. II of the Supplemental Material [99]). At the frequency of the reflectance peak of the Fabry-Perot

quasi-BIC $f_0 = 591.63 \text{ THz}$, the GH shift is significantly enhanced to $1266.6\lambda_0$ at the resonant angle $\theta = 3^\circ$.

It should be noted that the stationary-phase approach [i.e., Eq. (17)] is only applicable when the incident light beam is a quasiplane wave [34]. In Appendix, we perform the full-wave simulation to study the GH shift in the case of a Gaussian beam incidence via commercially available software COMSOL Multiphysics. Considering the limitation of the computer memory, we select $d = 100 \text{ nm}$ to simulate a moderate GH shift in the full-wave simulation. The simulated result shows that the GH shift in the case of a Gaussian beam incidence with a sufficiently large beam waist can reach the same order of magnitude of that calculated by Eq. (17).

Finally, we investigate the dependence of the peak value of the GH shift on the vertical distance between two single-layer gratings at $\theta = 3^\circ$ for TE polarization, as shown in Fig. 7(a). When the vertical distance between two single-layer gratings $d = 100 \text{ nm}$, the peak value of the GH shift is only $8.16 \times 10^1 \lambda_0$. As the vertical distance between two single-layer gratings gradually approaches d_{BIC} , the peak value of the GH shift increases rapidly. When the vertical distance between two single-layer gratings $d = 230 \text{ nm}$, the peak value of the GH shift reaches $2.05 \times 10^3 \lambda_0$. The underlying reason

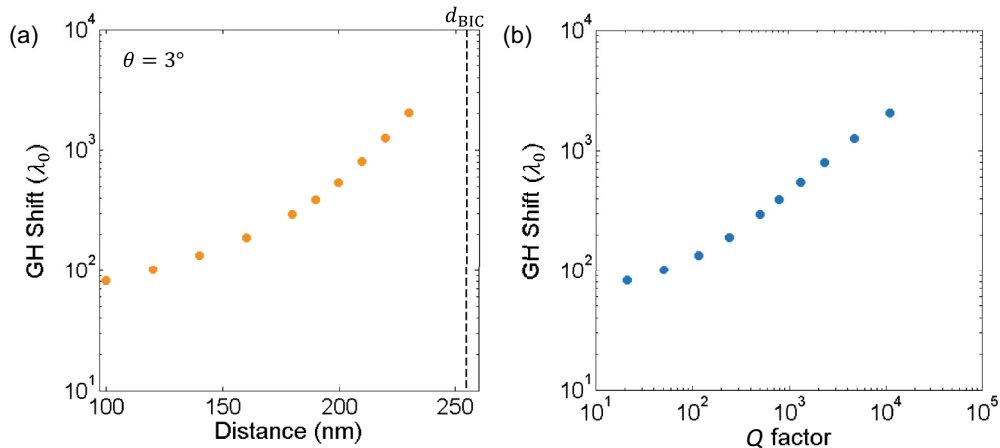


FIG. 7. (a) Dependence of the peak value of the GH shift on the vertical distance between two single-layer gratings at $\theta = 3^\circ$ for TE polarization. Black dashed line represents the vertical distance between two single-layer gratings for the Fabry-Perot BIC $d_{\text{BIC}} = 254.9 \text{ nm}$. (b) Dependence of the peak value of the GH shift on the Q factor of the Fabry-Perot quasi-BIC at $\theta = 3^\circ$ for TE polarization.

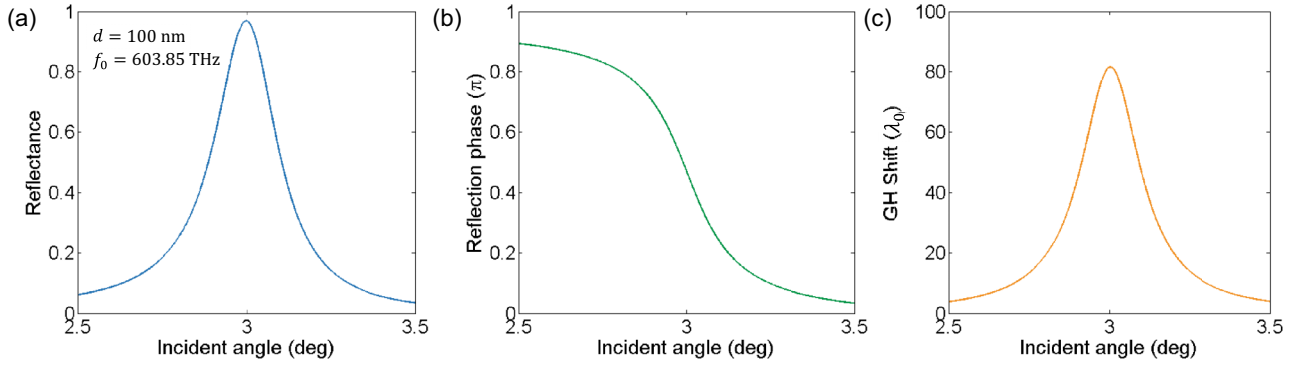


FIG. 8. (a) Reflectance, (b) reflection phase, and (c) GH shift angular spectra of the double-layer grating at the frequency of the reflectance peak of the Fabry-Perot quasi-BIC $f_0 = 603.85$ THz for TE polarization. The vertical distance between two single-layer gratings is set to be $d = 100$ nm.

of the increase in the peak value of the GH shift can be explained as follows. As the vertical distance between two single-layer gratings increases, the Q factor of the Fabry-Perot quasi-BIC increases rapidly (see Fig. 3). Hence, the full width at half maximum of the reflectance peak in the reflectance angular spectrum decreases, giving rise to larger GH shifts. Figure 7(b) gives the dependence of the peak value of the GH shift on the Q factor of the Fabry-Perot quasi-BIC. As the Q factor increases from 2.14×10^1 to 1.13×10^4 , the peak value of the GH shift increases from $8.16 \times 10^1 \lambda_0$ to $2.05 \times 10^3 \lambda_0$.

IV. CONCLUSIONS

In summary, we describe the optical response in double-layer gratings by a HCM comprising both near- and far-field couplings. The HCM indicates that the linewidths of two resonant modes in a double-layer grating are determined entirely by the far-field coupling strength. As the vertical distance between two single-layer gratings satisfies the Fabry-Perot resonant condition, the linewidth of one of the resonant modes vanishes, leading to a Fabry-Perot BIC. By changing the vertical distance between two single-layer gratings, the Q factor of the Fabry-Perot quasi-BIC can be tuned over a wide range. Driven by the angle-sensitive and ultrastrong resonant properties of the Fabry-Perot quasi-BIC, the GH shift can be significantly enhanced to the order of $10^3 \lambda_0$, together with high reflection. Our work provides a feasible recipe to observe quasi-BIC-driven giant GH shifts in experiments.

ACKNOWLEDGMENTS

This work is sponsored by the National Natural Science Foundation of China (Grants No. 12104105, No. 12364045, No. 12304420, No. 12264028, and No. 61805064), the Guangdong Basic and Applied Basic Research Foundation (Grant No. 2023A1515011024), the Science and Technology Program of Guangzhou (Grant No. 202201011176), the Natural Science Foundation of Jiangxi Province (Grants No. 20232BAB211025 and No. 20232BAB201040), the Young Elite Scientists Sponsorship Program by JXAST (Grant No. 2023QT11), the China Scholarship Council (Grant No. 202008420045), and the Start-up Funding of Guangdong Polytechnic Normal University (Grant No. 2021SDKYA033). F.W. thanks X. Qi from Tongji University for his kind help in the full-wave simulation.

APPENDIX: FULL-WAVE SIMULATION IN CASE OF GAUSSIAN BEAM INCIDENCE

In this appendix, we compare the GH shift calculated by the stationary-phase approach and that simulated by the full-wave simulation in the case of a Gaussian beam incidence. Considering the limitation of the computer memory, we select $d = 100$ nm to simulate a moderate GH shift in the full-wave simulation. Figure 8(a) gives the calculated reflectance angular spectrum of the double-layer grating at the frequency of the reflectance peak of the Fabry-Perot quasi-BIC $f_0 = 603.85$ THz for TE polarization. Owing to the angle-sensitive property of the Fabry-Perot quasi-BIC, an asymmetric

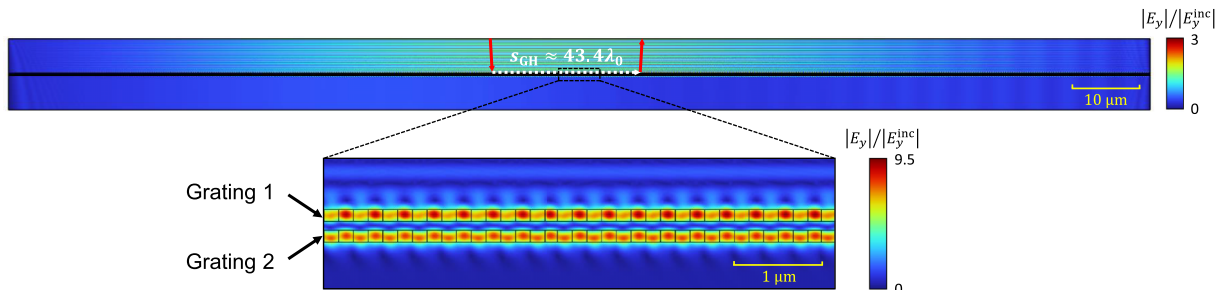


FIG. 9. Simulated electric field distribution in the case of a TE-polarized Gaussian beam incidence with an incident angle $\theta = 3^\circ$ and a frequency $f_0 = 603.85$ THz. The beam waist of the Gaussian beam is set to be $w = 120 \lambda_0$.

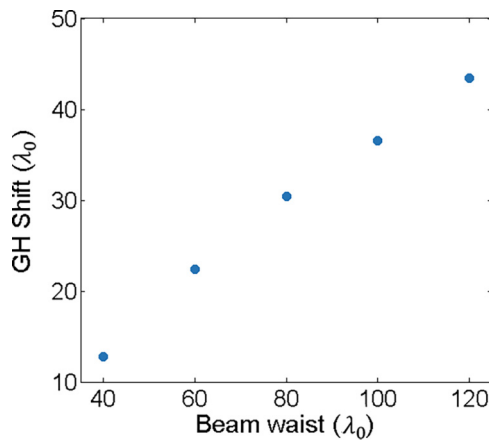


FIG. 10. Dependence of the simulated GH shift on the beam waist of the incident Gaussian beam.

Fano-like line shape occurs at the resonant angle $\theta = 3^\circ$ in the reflectance angular spectrum. In Fig. 8(b), we calculate the corresponding reflection phase angular spectrum. Obviously, the reflection phase changes sharply at the resonant angle $\theta = 3^\circ$. In Fig. 8(c), we calculate the corresponding GH shift angular spectrum. Owing to the sharp reflection phase change,

the calculated GH shift reaches $81.6\lambda_0$ at the resonant angle $\theta = 3^\circ$.

Then, we perform the full-wave simulation in the case of a TE-polarized Gaussian beam incidence with an incident angle $\theta = 3^\circ$ and a frequency $f_0 = 603.85$ THz. The beam waist of the Gaussian beam is set to be $w = 120\lambda_0$. The number of the unit cells of the double-layer grating is set to be $N = 500$. Figure 9 gives the simulated electric field distribution. The intensity of the local electric field is normalized to that of the incident electric field. The red arrows denote the central axes of the incident and reflected light beams. As demonstrated, the simulated GH shift can be extracted as $43.4\lambda_0$, which reaches the same order of magnitude of that calculated by the stationary-phase approach (i.e., $81.6\lambda_0$). Besides, the electric field is strongly localized inside two single-layer gratings, which is consistent to the results in Fig. 2(b).

Finally, we give the dependence of the simulated GH shift on the beam waist of the incident Gaussian beam, as shown in Fig. 10. As the beam waist of the incident Gaussian beam increases, the simulated GH shift becomes closer to that calculated by the stationary-phase approach. Specifically, as the beam waist of the incident Gaussian beam increases from $40\lambda_0$ to $120\lambda_0$, the simulated GH shift increases from $12.8\lambda_0$ to $43.4\lambda_0$.

-
- [1] F. Goos and H. Hänchen, Ein neuer und fundamentaler Versuch zur Totalreflexion, *Ann. Phys.* **436**, 333 (1947).
- [2] H. M. Lai, C. W. Kwok, Y. W. Loo, and B. Y. Xu, Energy-flux pattern in the Goos-Hänchen effect, *Phys. Rev. E* **62**, 7330 (2000).
- [3] P. R. Berman, Goos-Hänchen shift in negatively refractive media, *Phys. Rev. E* **66**, 067603 (2002).
- [4] C.-F. Li, Unified theory for Goos-Hänchen and Imbert-Fedorov effects, *Phys. Rev. A* **76**, 013811 (2007).
- [5] A. Aiello and J. P. Woerdman, Role of beam propagation in Goos-Hänchen and Imbert-Fedorov shifts, *Opt. Lett.* **33**, 1437 (2008).
- [6] K. Y. Bliokh, I. V. Shadrivov, and Y. S. Kivshar, Goos-Hänchen and Imbert-Fedorov shifts of polarized vortex beams, *Opt. Lett.* **34**, 389 (2009).
- [7] X. Chen, C.-F. Li, R.-R. Wei, and Y. Zhang, Goos-Hänchen shifts in frustrated total internal reflection studied with wave-packet propagation, *Phys. Rev. A* **80**, 015803 (2009).
- [8] A. Aiello, Goos-Hänchen and Imbert-Fedorov shifts: A novel perspective, *New J. Phys.* **14**, 013058 (2012).
- [9] K. Y. Bliokh and A. Aiello, Goos-Hänchen and Imbert-Fedorov shifts: An overview, *J. Opt.* **15**, 014001 (2013).
- [10] Y. Wong, Y. Miao, J. Skarda, and O. Solgaard, Large negative and positive optical Goos-Hänchen shift in photonic crystals, *Opt. Lett.* **43**, 2803 (2018).
- [11] G. Ye, W. Zhang, W. Wu, S. Chen, W. Shu, H. Luo, and S. Wen, Goos-Hänchen and Imbert-Fedorov effects in Weyl semimetals, *Phys. Rev. A* **99**, 023807 (2019).
- [12] W. Zhen and D. Deng, Goos-Hänchen shifts for Airy beams impinging on graphene-substrate surfaces, *Opt. Express* **28**, 24104 (2020).
- [13] Z. Chen, H. Zhang, X. Zhang, H. Li, W. Zhang, and L. Xi, Cross-coupling effect induced beam shifts for polarized vortex beam at two-dimensional anisotropic monolayer graphene surface, *Opt. Express* **28**, 8308 (2020).
- [14] T. Sakata, H. Togo, and F. Shimokawa, Reflection-type 2×2 optical waveguide switch using the Goos-Hänchen shift effect, *Appl. Phys. Lett.* **76**, 2841 (2000).
- [15] K. L. Tsakmakidis, A. D. Boardman, and O. Hess, Trapped rainbow storage of light in metamaterials, *Nature (London)* **450**, 397 (2007).
- [16] X. Wang, C. Yin, J. Sun, H. Li, Y. Wang, M. Ran, and Z. Cao, High-sensitivity temperature sensor using the ultrahigh order mode-enhanced Goos-Hänchen effect, *Opt. Express* **21**, 13380 (2013).
- [17] X. Wang, M. Sang, W. Yuan, Y. Nie, and H. Luo, Optical relative humidity sensing based on oscillating wave-enhanced Goos-Hänchen shift, *IEEE Photonics Technol. Lett.* **28**, 264 (2016).
- [18] H. Sattari, S. E. Bakhtevan, and M. Sahrai, Proposal for a 1×3 Goos-Hänchen shift-assisted de/multiplexer based on a multi-layer structure containing quantum dots, *J. Appl. Phys.* **120**, 133102 (2016).
- [19] T. Tang, J. Li, L. Luo, J. Shen, C. Li, J. Qin, L. Bi, and J. Hou, Weak measurement of magneto-optical Goos-Hänchen effect, *Opt. Express* **27**, 17638 (2019).
- [20] X. Jiao, Y. Cai, and Z. Wang, Goos-Hänchen and Imbert-Fedorov shifts of a laser beam reflected from ITO under complex fields, *Opt. Commun.* **457**, 124712 (2020).
- [21] X. Jiao, W. Liu, Z. Li, F. Sun, and L. Li, Voltage controllable Goos-Hänchen and Imbert-Fedorov shifts based on capacitor structure, *Opt. Mater.* **124**, 112003 (2022).

- [22] T. Tang, J. Li, Y. Mao, B. Liu, S. Peng, B. Yu, X. Liang, L. Luo, Y. Tang, and K. He, Beam shift modulation based on Larmor resonance in graphene-VO₂ photonic crystal, *Phys. Status Solidi B* **259**, 2100596 (2022).
- [23] S. Du, W. Zhang, W. Liu, Y. Zhang, M. Zhao, and L. Shi, Realization of large transmitted optical Goos-Hänchen shifts in photonic crystal slabs, *Nanophotonics* **11**, 4531 (2022).
- [24] S. Du, Z. Che, M. Zhao, W. Liu, and L. Shi, Realization of large transmitted Goos-Hänchen shifts with high (near 100%) transmittance based on a coupled double-layer grating system, *Opt. Lett.* **48**, 1710 (2023).
- [25] K. Artmann, Berechnung der Seitenversetzung des totalreflektierten Strahles, *Ann. Phys.* **437**, 87 (1948).
- [26] H. M. Lai and S. W. Chan, Large and negative Goos-Hänchen shift near the Brewster dip on reflection from weakly absorbing media, *Opt. Lett.* **27**, 680 (2002).
- [27] L. Wang, H. Chen, and S. Zhu, Large negative Goos-Hänchen shift from a weakly absorbing dielectric slab, *Opt. Lett.* **30**, 2936 (2005).
- [28] P. T. Leung, C. W. Chen, and H.-P. Chiang, Large negative Goos-Hänchen shift at metal surfaces, *Opt. Commun.* **276**, 206 (2007).
- [29] X. Yin, L. Hesselink, Z. Liu, N. Fang, and X. Zhang, Large positive and negative lateral optical beam displacements due to surface plasmon resonance, *Appl. Phys. Lett.* **85**, 372 (2004).
- [30] X. Yin and L. Hesselink, Goos-Hänchen shift surface plasmon resonance sensor, *Appl. Phys. Lett.* **89**, 261108 (2006).
- [31] V. J. Yallapragada, A. P. Ravishankar, G. L. Mulay, G. S. Agarwal, and V. G. Achanta, Observation of giant Goos-Hänchen and angular shifts at designed metasurfaces, *Sci. Rep.* **6**, 19319 (2016).
- [32] Y. Wang, Y. Hu, R. Xie, Q. Zeng, Y. Hong, X. Chen, P. Zhang, L. Zeng, Y. Zhang, S. Zeng, and H. Yang, Ultrasensitive label-free miRNA-21 detection based on MXene-enhanced plasmonic lateral displacement measurement, *Nanophotonics* **12**, 4055 (2023).
- [33] C.-F. Li and Q. Wang, Prediction of simultaneously large and opposite generalized Goos-Hänchen shifts for TE and TM light beams in an asymmetric double-prism configuration, *Phys. Rev. E* **69**, 055601(R) (2004).
- [34] L. Wang and S. Zhu, Giant lateral shift of a light beam at the defect mode in one-dimensional photonic crystals, *Opt. Lett.* **31**, 101 (2006).
- [35] K. V. Sreekanth, Q. Ouyang, S. Han, K.-T. Yong, and R. Singh, Giant enhancement of Goos-Hänchen shift at the singular phase of a nanophotonic cavity, *Appl. Phys. Lett.* **112**, 161109 (2018).
- [36] I. V. Soboleva, V. V. Moskalenko, and A. A. Fedyanin, Giant Goos-Hänchen effect and Fano resonance at photonic crystal surfaces, *Phys. Rev. Lett.* **108**, 123901 (2012).
- [37] Y. Wan, Z. Zheng, W. Kong, X. Zhao, Y. Liu, Y. Bian, and J. Liu, Nearly three orders of magnitude enhancement of Goos-Hänchen shift by exciting Bloch surface wave, *Opt. Express* **20**, 8998 (2012).
- [38] J. Tang, J. Xu, Z. Zheng, H. Dong, J. Dong, S. Qian, J. Guo, L. Jiang, and Y. Xiang, Graphene Tamm plasmon-induced giant Goos-Hänchen shift at terahertz frequencies, *Chin. Opt. Lett.* **17**, 020007 (2019).
- [39] J. Wu, F. Wu, K. Lv, Z. Guo, H. Jiang, Y. Sun, Y. Li, and H. Chen, Giant Goos-Hänchen shift with a high reflectance assisted by interface states in photonic heterostructures, *Phys. Rev. A* **101**, 053838 (2020).
- [40] Y. Ye, W. Chen, S. Wang, Y. Liu, and L. Jiang, Enhanced and tunable Goos-Hänchen effect of reflected light due to Tamm surface plasmons with Dirac semimetals, *Results Phys.* **43**, 106105 (2022).
- [41] C. W. Hsu, B. Zhen, A. D. Stone, J. D. Joannopoulos, and M. Soljačić, Bound state in the continuum, *Nat. Rev. Mater.* **1**, 16048 (2016).
- [42] S. Joseph, S. Pandey, S. Sarkar, and J. Joseph, Bound states in the continuum in resonant nanostructures: An overview of engineered materials for tailored applications, *Nanophotonics* **10**, 4175 (2021).
- [43] S. I. Azzam and A. V. Kildishev, Photonic bound states in the continuum: From basics to applications, *Adv. Opt. Mater.* **9**, 2001469 (2021).
- [44] A. F. Sadreev, Interference traps waves in an open system: Bound states in the continuum, *Rep. Prog. Phys.* **84**, 055901 (2021).
- [45] S. S. Biswas, G. Remesh, V. G. Achanta, A. Banerjee, N. Ghosh, and S. D. Gupta, Enhanced beam shifts mediated by bound states in the continuum, *J. Opt.* **25**, 095401 (2023).
- [46] C. W. Hsu, B. Zhen, J. Lee, S. Chua, S. G. Johnson, J. D. Joannopoulos, and M. Soljačić, Observation of trapped light within the radiation continuum, *Nature (London)* **499**, 188 (2013).
- [47] Y. Yang, C. Peng, Y. Liang, Z. Li, and S. Noda, Analytical perspective for bound states in the continuum in photonic crystal slabs, *Phys. Rev. Lett.* **113**, 037401 (2014).
- [48] J. Jin, X. Yin, L. Ni, M. Soljačić, B. Zhen, and C. Peng, Topologically enabled ultrahigh-*Q* guided resonances robust to out-of-plane scattering, *Nature (London)* **574**, 501 (2019).
- [49] C. Zhao, W. Chen, J. Wei, W. Deng, Y. Yan, Y. Zhang, and C.-W. Qiu, Electrically tunable and robust bound states in the continuum enabled by 2D transition metal dichalcogenide, *Adv. Opt. Mater.* **10**, 2201634 (2022).
- [50] P. Hu, J. Wang, Q. Jiang, J. Wang, L. Shi, D. Han, Z. Q. Zhang, C. T. Chan, and J. Zi, Global phase diagram of bound states in the continuum, *Optica* **9**, 1353 (2022).
- [51] K. Koshelev, S. Lepeshov, M. Liu, A. Bogdanov, and Y. Kivshar, Asymmetric metasurfaces with high-*Q* resonances governed by bound states in the continuum, *Phys. Rev. Lett.* **121**, 193903 (2018).
- [52] X. Jiang, B. Fang, and C. Zhan, Theoretical enhancement of the Goos-Hänchen shift with a metasurface based on bound states in the continuum, *Micromachines* **14**, 1109 (2023).
- [53] J. Zhang, Y. Ruan, Z.-D. Hu, J. Wu, and J. Wang, An enhanced high *Q*-factor resonance of quasi-bound states in the continuum with all-dielectric metasurface based on multilayer film structures, *IEEE Sensors J.* **23**, 2070 (2023).
- [54] Z. Huang, W. Liu, Z. Wei, H. Meng, H. Liu, J. Guo, Y. Zhi, L. Xiang, H. Li, and F. Wang, Giant enhancement of the Goos-Hänchen shift based on quasi-bound states in the continuum in terahertz band through silicon based metasurface, *Opt. Commun.* **540**, 129507 (2023).
- [55] S. Chen, Z. Li, Y. Mao, X. Dai, and Y. Xiang, Giant enhancement of the Goos-Hänchen shift assisted by merging bound states in the continuum, *J. Appl. Phys.* **133**, 193101 (2023).

- [56] W. Wang, Y. K. Srivastava, T. C. Tan, Z. Wang, and R. Singh, Brillouin zone folding driven bound states in the continuum, *Nat. Commun.* **14**, 2811 (2023).
- [57] W. Chen, Y. Li, Y. Liu, Y. Gao, Y. Yan, Z. Dong, and J. Zhu, All-dielectric Sers metasurfaces with strong coupling quasi-BIC energized by transformer-based deep learning, *Adv. Opt. Mater.* **12**, 2301697 (2023).
- [58] H. M. Doeleman, F. Monticone, W. den Hollander, A. Alù, and A. F. Koenderink, Experimental observation of a polarization vortex at an optical bound state in the continuum, *Nat. Photon.* **12**, 397 (2018).
- [59] T. Ning, X. Li, Y. Zhao, L. Yin, Y. Huo, L. Zhao, and Q. Yue, Giant enhancement of harmonic generation in all-dielectric resonant waveguide gratings of quasibound states in the continuum, *Opt. Express* **28**, 34024 (2020).
- [60] W. Shi, J. Gu, X. Zhang, Q. Xu, J. Han, Q. Yang, L. Cong, and W. Zhang, Terahertz bound states in the continuum with incident angle robustness induced by a dual period metagrating, *Photon. Res.* **10**, 810 (2022).
- [61] J. Liu, C. Chen, X. Li, J. Li, D. Dong, Y. Liu, and Y. Fu, Tunable dual quasi-bound states in continuum and electromagnetically induced transparency enabled by the broken material symmetry in all-dielectric compound gratings, *Opt. Express* **31**, 4347 (2023).
- [62] J. Hu, H. Guan, X. Liu, D. Ren, and J. Zhao, High-performance gas sensor with symmetry-protected quasi-bound states in the continuum, *Opt. Express* **31**, 36228 (2023).
- [63] X. Gu, X. Liu, X.-F. Yan, W.-J. Du, Q. Lin, L.-L. Wang, and G.-D. Liu, Polaritonic coherent perfect absorption based on self-hybridization of a quasi-bound state the in continuum and exciton, *Opt. Express* **31**, 4691 (2023).
- [64] F. Wu, T. Liu, Y. Long, S. Xiao, and G. Chen, Giant photonic spin Hall effect empowered by polarization-dependent quasi-bound states in the continuum in compound grating waveguide structures, *Phys. Rev. B* **107**, 165428 (2023).
- [65] D. N. Maksimov, V. S. Gerasimov, S. Romano, and S. P. Polyotov, Refractive index sensing with optical bound states in the continuum, *Opt. Express* **28**, 38907 (2020).
- [66] D. N. Maksimov, V. S. Gerasimov, A. A. Bogdanov, and S. P. Polyotov, Enhanced sensitivity of an all-dielectric refractive index sensor with an optical bound state in the continuum, *Phys. Rev. A* **105**, 033518 (2022).
- [67] M. V. Gorkunov, A. A. Antonov, and Y. S. Kivshar, Metasurfaces with maximum chirality empowered by bound states in the continuum, *Phys. Rev. Lett.* **125**, 093903 (2020).
- [68] T. Shi, Z.-L. Deng, G. Geng, X. Zeng, Y. Zeng, G. Hu, A. Overvig, J. Li, C.-W. Qiu, A. Alù, Y. Kivshar, and X. Li, Planar chiral metasurfaces with maximal and tunable chiroptical response driven by bound states in the continuum, *Nat. Commun.* **13**, 4111 (2022).
- [69] X. Zhang, Y. Liu, J. Han, Y. Kivshar, and Q. Song, Chiral emission from resonant metasurfaces, *Science* **377**, 1215 (2022).
- [70] Y. Chen, H. Deng, X. Sha, W. Chen, R. Wang, Y.-H. Chen, D. Wu, J. Chu, Y. S. Kivshar, S. Xiao, and C.-W. Qiu, Observation of intrinsic chiral bound states in the continuum, *Nature (London)* **613**, 474 (2023).
- [71] S. Xiao, M. Qin, J. Duan, F. Wu, and S. Xiao, Polarization-controlled dynamically switchable high-harmonic generation from all-dielectric metasurfaces governed by dual bound states in the continuum, *Phys. Rev. B* **105**, 195440 (2022).
- [72] T. Liu, M. Qin, F. Wu, and S. Xiao, High-efficiency optical frequency mixing in an all-dielectric metasurface enabled by multiple bound states in the continuum, *Phys. Rev. B* **107**, 075441 (2023).
- [73] S. Feng, T. Liu, W. Chen, F. Wu, and S. Xiao, Enhanced sum-frequency generation from etchless lithium niobate empowered by dual quasi-bound states in the continuum, *Sci. China: Phys. Mech. Astron.* **66**, 124214 (2023).
- [74] F. Wu, J. Wu, Z. Guo, H. Jiang, Y. Sun, Y. Li, J. Ren, and H. Chen, Giant enhancement of the Goos-Hänchen shift assisted by quasibound states in the continuum, *Phys. Rev. Appl.* **12**, 014028 (2019).
- [75] F. Wu, M. Luo, J. Wu, C. Fan, X. Qi, Y. Jian, D. Liu, S. Xiao, G. Chen, H. Jiang, Y. Sun, and H. Chen, Dual quasi-bound states in the continuum in compound grating waveguide structures for large positive and negative Goos-Hänchen shifts with perfect reflection, *Phys. Rev. A* **104**, 023518 (2021).
- [76] Y. Ruan, Y. Li, Z. Hu, J. Wang, and Y. Wang, Strong resonance response with ultrahigh quality factor in grating-multilayer systems based on quasi-bound states in the continuum, *Sci. Rep.* **12**, 21471 (2022).
- [77] Y. Ruan, Z.-D. Hu, J. Wang, L. Yu, and Y. Wang, Adjacent asymmetric tilt grating structure with strong resonance assisted by quasi-bound states in the continuum, *IEEE Photon. J.* **14**, 4655906 (2022).
- [78] F. Wu, X. Qi, M. Qin, M. Luo, Y. Long, J. Wu, Y. Sun, H. Jiang, T. Liu, S. Xiao, and H. Chen, Momentum mismatch driven bound states in the continuum and ellipsometric phase singularities, *Phys. Rev. B* **109**, 085436 (2024).
- [79] R. Jin, L. Huang, C. Zhou, J. Guo, Z. Fu, J. Chen, J. Wang, X. Li, F. Yu, J. Chen, Z. Zhao, X. Chen, W. Lu, and G. Li, Toroidal dipole BIC-driven highly robust perfect absorption with a graphene-loaded metasurface, *Nano Lett.* **23**, 9105 (2023).
- [80] W. Suh, M. Y. Yanik, O. Solgaard, and S. Fan, Displacement-sensitive photonic crystal structures based on guided resonance in photonic crystal slab, *Appl. Phys. Lett.* **82**, 1999 (2003).
- [81] D. C. Marinica and A. G. Borisov, Bound states in the continuum in photonics, *Phys. Rev. Lett.* **100**, 183902 (2008).
- [82] E. N. Bulgakov, D. N. Maksimov, P. N. Semina, and S. A. Skorobogatov, Propagating bound states in the continuum in dielectric gratings, *J. Opt. Soc. Am. B* **35**, 1218 (2018).
- [83] H. Hemmati and R. Magnusson, Resonant dual-grating metamembranes supporting spectrally narrow band states in the continuum, *Adv. Opt. Mater.* **7**, 1900754 (2019).
- [84] F. Wu, C. Fan, K. Zhu, J. Wu, X. Qi, Y. Sun, S. Xiao, H. Jiang, and H. Chen, Tailoring electromagnetic responses in a coupled-grating system with combined modulation of near-field and far-field couplings, *Phys. Rev. B* **105**, 245417 (2022).
- [85] M. Luo and F. Wu, Wavy optical grating: Wideband reflector and Fabry-Pérot bound states in the continuum, *Phys. Rev. A* **106**, 063514 (2022).
- [86] H. Zhang, T. Wang, J. Tian, J. Sun, S. Li, I. De Leon, R. P. Zaccaria, L. Peng, F. Gao, X. Lin, H. Chen, and G. Wang, Quasi-BIC laser enabled by high-contrast grating resonator for gas detection, *Nanophotonics* **11**, 297 (2022).
- [87] J. Wu, J. Chen, X. Qi, Z. Guo, J. Wang, F. Wu, Y. Sun, Y. Li, H. Jiang, L. Shi, J. Zi, and H. Chen, Observation of accurately

- designed bound states in the continuum in momentum space, *Photon. Res.* (2024), doi:10.1364/PRJ.515969.
- [88] H. Xu and Y. Shi, Silicon-waveguide-integrated high-quality metagrating supporting bound state in the continuum, *Laser Photon. Rev.* **14**, 1900430 (2020).
- [89] F. Monticone, H. M. Doeleman, W. D. Hollander, A. F. Koenderink, and A. Alù, Trapping light in plain sight: Embedded photonic eigenstates in zero-index metamaterials, *Laser Photon. Rev.* **12**, 1700220 (2018).
- [90] D. V. Novitsky, A. S. Shalin, D. Redka, V. Bobrovs, and A. V. Novitsky, Quasibound states in the continuum induced by PT -symmetry breaking, *Phys. Rev. B* **104**, 085126 (2021).
- [91] Z. S. Liu, S. Tibuleac, D. Shin, P. P. Young, and R. Magnusson, High-efficiency guided-mode resonance filter, *Opt. Lett.* **23**, 1556 (1998).
- [92] Y. Sun, W. Tan, H.-q. Li, J. Li, and H. Chen, Experimental demonstration of a coherent perfect absorber with PT phase transition, *Phys. Rev. Lett.* **112**, 143903 (2014).
- [93] B. Peng, Ş. K. Özdemir, S. Rotter, H. Yilmaz, M. Liertzer, F. Monifi, C. M. Bender, F. Nori, and L. Yang, Loss-induced suppression and revival of lasing, *Science* **346**, 328 (2014).
- [94] W. Tan, Y. Sun, Z.-G. Wang, and H. Chen, Manipulating electromagnetic responses of metal wires at the deep subwavelength scale via both near- and far-field couplings, *Appl. Phys. Lett.* **104**, 091107 (2014).
- [95] S. Fan, W. Suh, and J. D. Joannopoulos, Temporal coupled-mode theory for the Fano resonance in optical resonators, *J. Opt. Soc. Am. A* **20**, 569 (2003).
- [96] M. G. Moharam, D. A. Pomett, E. B. Grann, and T. K. Gaylord, Stable implementation of the rigorous coupled-wave analysis for surface-relief gratings: Enhanced transmittance matrix approach, *J. Opt. Soc. Am. A* **12**, 1077 (1995).
- [97] L. Gu, H. Fang, J. Li, L. Fang, S. J. Chua, J. Zhao, and X. Gan, A compact structure for realizing Lorentzian, Fano and electromagnetically induced transparency resonance lineshapes in a microring resonator, *Nanophotonics* **8**, 841 (2019).
- [98] Y. S. Joe, A. M. Satanin, and C. S. Kim, Classical analogy of Fano resonances, *Phys. Scr.* **74**, 259 (2006).
- [99] See Supplemental Material at <http://link.aps.org/supplemental/10.1103/PhysRevB.109.125411> for the reflectance spectrum of the double-layer grating when shifting the bottom single-layer grating in plane; the GH shift when the vertical distance between two single-layer gratings is $d = 220$ nm.